Effect of discrete macroion charge distributions in solutions of like-charged macroions

Khawla Qamhieh and Per Linse

Articles you may be interested in

Effects of image charges, interfacial charge discreteness, and surface roughness on the zeta potential of spherical electric double layers
J. Chem. Phys. **137**, 034708 (2012); 10.1063/1.4736570

Dressed molecule theory for liquids and solutions: An exact charge renormalization formalism for molecules with arbitrary charge distributions
J. Chem. Phys. **119**, 11380 (2003); 10.1063/1.1623179

Structure, phase stability, and thermodynamics in charged colloidal solutions
J. Chem. Phys. **113**, 4359 (2000); 10.1063/1.1288022

Forces between like-charged walls in an electrolyte solution: A comparison of McMillan–Mayer results for several models
J. Chem. Phys. **113**, 2851 (2000); 10.1063/1.1305823

Electrostatic attraction and phase separation in solutions of like-charged colloidal particles
J. Chem. Phys. **112**, 3917 (2000); 10.1063/1.480943

Effect of discrete macroion charge distributions in solutions of like-charged macroions

Khawla Qamhieh[a)]
Physics Department, College of Science and Technology, Al-Quds University, Jerusalem, Palestine

Per Linse
*Physical Chemistry1, Center for Chemistry and Chemical Engineering, Lund University, P.O. Box 124,
SE-221 00 Lund, Sweden*

The effect of replacing the conventional uniform macroion surface charge density with discrete macroion charge distributions on structural properties of aqueous solutions of like-charged macroions has been investigated by Monte Carlo simulations. Two discrete charge distributions have been considered: point charges localized on the macroion surface and finite-sized charges protruding into the solution. Both discrete charge distributions have been examined with fixed and mobile macroion charges. Different boundary conditions have been applied to examine various properties. With point charges localized on the macroion surface, counterions become stronger accumulated to the macroion and the effect increases with counterion valence. As a consequence, with mono- and divalent counterions the potential of mean force between two macroions becomes less repulsive and with trivalent counterions more attractive. With protruding charges, the excluded volume effect dominates over the increased correlation ability; hence the counterions are less accumulated near the macroions and the potential of mean force between two macroions becomes more repulsive/less attractive. © *2005 American Institute of Physics*. [DOI: 10.1063/1.1979496]

I. INTRODUCTION

Charged colloids in solution are ubiquitous in a wide variety of biological and technical systems. Some examples are globular proteins made by amino acids, micelles formed by charged surfactants or charged block copolymers, micro-emulsions formed by water, oil, and charged surfactants, silica particles made by silica oxide, and polystyrene-based latex particles. Physicochemical properties of solutions of charged colloids are to a large degree controlled by electrostatic interactions.[1,2]

The primitive model of electrolytes constitutes a firm basis for examining the distribution of small ions near charged colloids as well as as the intercolloidal structure of colloidal solutions. In this model, the charged colloids (referred to as macroions) and the small ions are both represented as hard spheres with central charges, whereas the solvent is treated as a dielectric medium. Much of the recent theoretical and simulation advances are summarized in several reviews.[3–7]

Regarding solutions of charged macroions, (i) the accumulations of oppositely charged small ions near the macroions and (ii) the appearance of an effective repulsion of electrostatic origin between like-charged colloids, which at certain conditions can turn into an effective colloidal attraction, are two fundamental observations. The accumulation of counterions and the effective repulsion are issues captured by the Poisson-Boltzmann (PB) theory.[1] For example, the linearized PB theory constitutes one of the two components

in the celebrated Derjaguin-Landau-Verwey-Overbeek theory,[8,9] which was a major theoretical step for rationalizing colloidal stability taken in the 1940s. Four decades later, studies using simulation techniques[10] and liquid-state theories[11] demonstrated the existence of an attraction of electrostatic nature between two like-charged planar surfaces originating from ion-ion correlations. Attraction between like-charged macroions of the same origin was later confirmed by several simulation studies[12–24] and theoretically predicted in the limit of strong electrostatic coupling.[25]

Another point of departure to describe colloidal solutions is to make a full atomic description. Such approaches have been taken to describe a single colloid formed by self-associating surfactants[26,27] and provide a wealth of details on the internal structure and dynamics as well as on the hydration. However, concern has to be taken to establish a description where the electrostatic and hydrophobic interactions are balanced in an appropriate manner.

Returning to the primitive model for describing charged colloids, different types of extensions have been proposed. One of them involves the inclusion of charge polarization appearing at the colloid-solvent interface when taking into account the lower permittivity inside the colloid.[28–30] Another extension comprises the replacement of the homogeneous surface charge density with discrete macroion charges to represent surfactant micells[29,31,32] and globular proteins.[33,34]

The goal of the present contribution is to more firmly understand the effects of different macroion charge distributions on some properties of solutions containing macroions and their counterions. In addition to the central macroion

---
a)Author to whom correspondence should be addressed. Electronic mail:
khawla@gmail.com

charge, two discrete macroion charge distributions are considered; one where point charges are localized on the macroion surface and one where the finite-sized charges possess a hard-sphere radius and protrude into the solution. Moreover, both discrete charged distributions were examined for fixed and mobile charges. Various properties have been analyzed employing three different boundary conditions including (i) the accumulation of counterions near a macroion and the macroion charge structure using a spherical cell, (ii) the mean force and the potential of mean force between two macroions using a cylindrical cell, and (iii) the structure and the stability of bulk solution using a cubic box.

In a recent paper by Messina, he investigated the effects of macroion charge discretization for spherical macroions, where the macroion charges were randomly distributed on the macroion surface. He employed a spherical cell and reported on the distribution of the counterions with a focus on an infinite and on very large electrostatic coupling. The present contribution differs from that by Messina with respect that we throughout cover electrostatic coupling conditions relevant for aqueous solution at ambient temperature and include consequences on the macroion interaction and bulk structure.

II. MODEL AND METHOD

A. Model

Consider solutions of charged spherical macroions and counterions. Throughout, macroions are represented as hard spheres with radius $R_M=20$ Å and a total charge $Z_M=-60$, originating from $N_S=60$ charged sites with radius R_S and charge $Z_S=-1$. In total, five different macroion models will be considered. The counterions are represented by charged hard spheres with radius $R_I=2$ Å and charge $Z_I=+1$, $+2$, or $+3$.

Three different types of macroion charge distributions have been considered, of which two are further divided into two cases. (1) In the *central* (C) charge distribution, all N_S charges are localized at the center of the macroion [see Fig. 1(a)]. Hence, in practice the conventional case with a single interaction size, here with charge $Z_M=-60$, localized at the center of the macroion is recovered. As to the electrostatic field at $r>R_M$, by Gauss theorem this charge distribution is equivalent to a homogeneous surface charge density $\sigma_M=eZ_M/4\pi R_M^2$ at $r=R_M$. (2) In the *surface* (S) charge distribution, the N_S charges are positioned at the distance $r_S=R_M$ from the center of the macroion, hence the macroion charges are exactly localized on the hard-sphere surface of the macroion [see Fig. 1(b), left]. The macroion charges have no extension, i.e., $R_S=0$, and thus the macroion surface is smooth. (3) In the *protruding* (P) charge distribution, the N_S charges are positioned at the distance $r_S=R_M+R_S$ from the center of the macroion with $R_S=2$ Å, where R_S is also the hard-sphere radius of the macroion charges [see Fig. 1(b), right]. Hence, the macroion charges are positioned 2 Å outside the hard-sphere surface and are protruding 4 Å into the solution. As to the surface and protruding charge distributions, two different cases have been considered. In the *frozen* (F) arrangement, the charges are immobile and their distri-
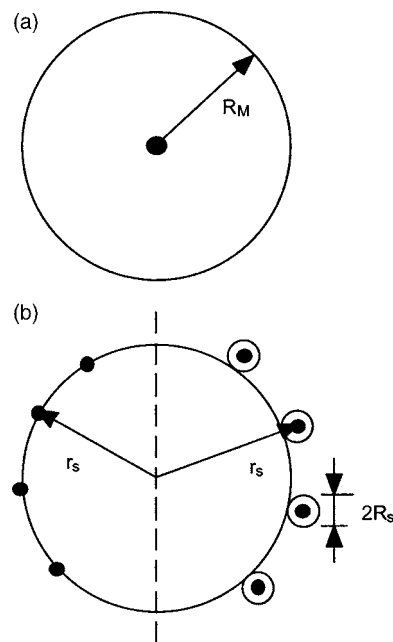

FIG. 1. Two-dimensional schematic illustration of the macroion charge distributions: (a) a central charge with R_M denoting the macroion radius, (b, left) point charges on the macroion surface, and (b, right) protruding charges with hard-sphere radius R_S. In (b), r_S denotes the radial location of the macroion charges.

bution is selected to be isomorphic to that of the carbon positions in the fullerene C_{60} molecule [see Fig. 2(a)], whereas in the *mobile* (M) arrangement, the charges are laterally mobile at the distance r_S [see Fig. 2(b)]. The characteristic separation between two neighboring macroion charges becomes ≈ 8 Å. Table I comprises a description of the five different macroion models.

Three different types of boundary conditions and number of macroions have been employed: (1) a spherical cell with radius $R_{sph}=100$ Å $(5R_M)$ containing one macroion $(N_M=1)$ at the center of the cell, (2) a cylindrical cell with radius $R_{cyl}=80$ Å $(4R_M)$ and length $L_{cyl}=398$ Å $(19.9R_M)$ containing two macroions $(N_M=2)$, symmetrically placed on the C_∞-symmetry axis, and (3) a cubic box with a box length $L_{box}=543$ Å and 40 macroions $(N_M=40)$ where periodic boundary conditions are applied. At all different boundary conditions, electroneutrality was established by supplying relevant amount of counterions, $N_I=|Z_M/Z_I|N_M$. In the cell approaches, the solution inside a cell is electrostatically decoupled from the surrounding. In this way, a complicated many-body problem is reduced to an effective one; here to an effective one-macroion (spherical cell) or an effective two-macroion (cylindrical cell) problem.

In more detail, the total potential energy of the system U is

$$U = U_{hs} + U_{elec} + U_{ext}, \qquad (1)$$

where the hard-sphere repulsion U_{hs} is given by

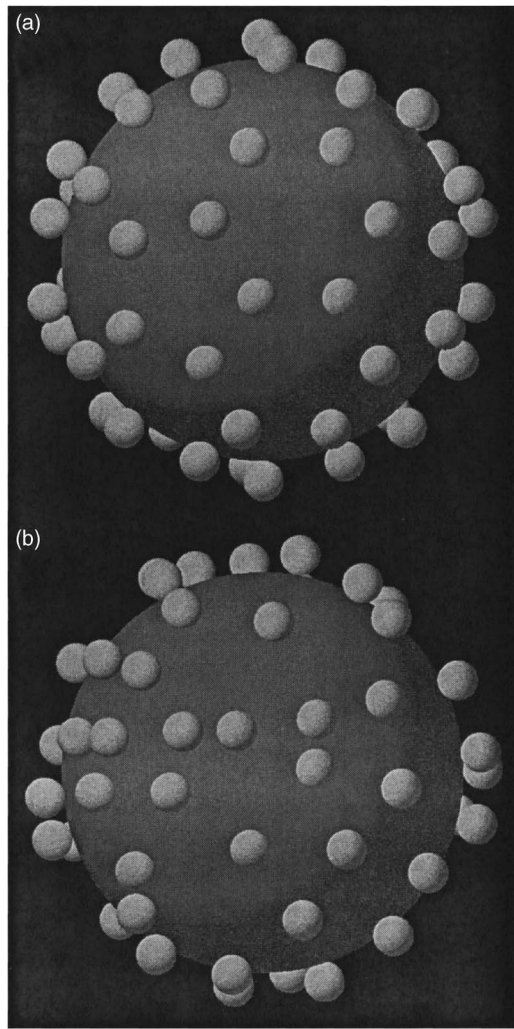$$U_{hs} = \sum_{i<j} u_{ij}^{hs}(r_{ij}), \qquad (2)$$

FIG. 2. Illustration of (a) frozen protruding and (b) mobile protruding charge distributions. In (b), a representative charge distribution with monovalent counterions is shown, and note that the counterions are not displayed.

$$u_{ij}^{hs}(r_{ij}) = \begin{cases} \infty, & r_{ij} < R_i + R_j \\ 0, & r_{ij} \geq R_i + R_j \end{cases} \tag{3}$$

with R_i denoting the radius of particle i (a macroion, a macroion site, or a counterion) and r_{ij} the distance between the centers of particles i and j. The Coulomb interaction U_{elec} is given by

$$U_{elec} = \sum_{i<j} u_{ij}^{elec}(r_{ij}), \tag{4}$$

$$u_{ij}^{elec}(r_{ij}) = \frac{Z_i Z_j e^2}{4\pi\varepsilon_0\varepsilon_r r_{ij}}, \tag{5}$$

where Z_i is the charge of particle i (a macroion site or a counterion), e the elementary charge, ε_0 the permittivity of vacuum, and ε_r the relative permittivity of water.

Finally, the confinement potential energy U_{ext} in Eq. (1) is given by

TABLE I. Overview of macroion models. Common: $N_S=60$, $Z_S=-1$, $R_M = 20$ Å, and $Z_M=N_S Z_S=-60$.

Label	Charge distribution	R_S (Å)	r_S (Å)	Lateral mobility
C	Central charge[a]	0	0	...
FS	Frozen surface charges	0	20	No[b]
MS	Mobile surface charges	0	20	Yes[c]
FP	Frozen protruding charges	2[d]	22	No[b]
MP	Mobile protruding charges	2[d]	22	Yes[c]

[a]Equivalent to a homogeneous macroion surface charge density $\sigma_M = eZ_M/4\pi R_M^2$ at $r=R_M$.
[b]Macroion charges are immobile on the surface $r=r_S$ in a configuration analogous to the C_{60} fullerene.
[c]Macroion charges are mobile on the surface $r=r_S$.
[d]Macroion charges protrude $2R_S=4$ Å from the hard-sphere surface.

$$U_{ext} = \sum_i u^{ext}(r_i) \tag{6}$$

with

$$u^{ext}(r_i) = \begin{cases} 0, & r_i \leq R_{sph} \\ \infty, & r_i > R_{sph} \end{cases} \tag{7}$$

for the spherical cell, whereas

$$u^{ext}(r_i) = \begin{cases} 0, & \sqrt{(x_i^2 + y_i^2)} \leq R_{cyl} \text{ and } |z_i| \leq L_{cyl}/2 \\ \infty, & \text{otherwise} \end{cases} \tag{8}$$

for the cylindrical cell. Formally, the confinement potential acts on all particles, but in practice only on the counterions.

Throughout, all systems are considered at the macroion number density $\rho_M = 2.5 \times 10^{-7}$ Å^{-3}, corresponding to a macroion volume fraction $\phi_M = 0.0084$. The temperature $T = 298$ K and the relative permittivity $\varepsilon_r = 78.4$ were used. At these conditions, the Bjerrum length, denoting the distance between two unit charges at which the Coulomb interaction is equal to the thermal energy, becomes 7.15 Å.

B. Simulation details

The models were solved by performing Monte Carlo (MC) simulation in the canonical ensemble (constant number of particles, volume, and temperature) according to the standard Metropolis algorithm with some extensions described below. The potential energies were evaluated using Eqs. (1)–(8). In the spherical and cylindrical cell approaches, all interactions were included; hence no potential cutoff was used. In the cubic box, periodic boundary conditions were applied and the long-range Coulomb interaction was handled by using the Ewald summation technique.[35–37]

Initial configurations were generated by first placing the macroion(s) in the center of the spherical cell, symmetrically on the C_∞ axis of the cylindrical cell, or randomly in the cubic box. Thereafter, the macroion charges were positioned according to the different charge distributions; in the case of mobile charges randomly on the surface $r=r_s$. Finally, the counterions were positioned randomly. Throughout, checks for hard-sphere overlap were made.

Several types of trial displacements were applied. At all the three boundary conditions, (i) trial rotation of macroions (frozen macroion charges) or lateral trail displacement of

single macroion charges (mobile macroion charges) and (ii) trial displacement of counterions were made. In addition, for the cylindrical cell approach trial displacements of macroions along the z axis were made, and the z coordinates of all particles were adjusted such that the positions of the macroions remained symmetrically with respect to $z=0$. For the cubic box, additional trail displacements of the macroions in all three dimensions were made. These translational displacements of macroions were augmented with the cluster moves, where counterions within some distance from the selected macroion were also subjected to the same trial displacement.[7,38,39] With trivalent counterions, an effective attraction mediated by the counterions operates between macroions leading to a physical clustering of the macroions. Further details of the equilibration of these systems, including the use of a second-level cluster move,[7] are given in the Appendix. Throughout, the Metropolis acceptance criterion was adapted to ensure the fulfillment of the detailed balance condition.

After equilibration, production runs involved typically 10×10^5 (spherical cell), 10×10^5 (cylindrical cell), and 4×10^5 (cubic box) trail moves per particles. Error estimates of means were made by extrapolation of means of sub-batches to infinite-sized batches. All the simulations were performed using the integrated Monte Carlo/molecular-dynamics/Brownian dynamics simulation package MOLSIM.[40]

C. Mean force and potential of mean force

The cylindrical cell approach has previously been employed to calculate effective interactions between two macroions.[22,24] The effective interaction depends on the cell volume[22] though the counterion entropy. The cylindrical cell approach rests on the assumption that the effective interaction is at most weakly dependent on the shape of the cylindrical cell. This assumption has been found to be valid for similar systems.[22]

The mean force F operating on one of the macroions, say, M, projected on the macroion-macroion intermacroion vector $\mathbf{r}_{MM}$ (below simplified to r) is defined by

$$F(r) \equiv \sum_{i \in M} \sum_{j \notin M} \langle -\nabla_{r_{ij}} u_{ij}(r_{ij}) \rangle \qquad (9)$$

with $F(r) > 0$ implying a repulsive and $F(r) < 0$ an attractive mean force and $\langle \cdots \rangle$ denoting an ensemble average of particle positions. The related potential of mean force (pmf) $U^{pmf}(r)$ is defined by

$$U^{pmf}(r) \equiv -\int_{\infty}^{r} F(r') dr'. \qquad (10)$$

Conventionally, $F(r)$ and $U^{pmf}(r)$ approach zero at large r.

Since the macroions and their counterions are confined in a cell, which approximately takes into account the influence of the surrounding electrolyte, the force is a mean force rather than an effective one.[5] In the corresponding fluid, the macroion-macroion mean force is the force acting between two macroions averaged over the positions of surrounding counterions and macroions and is directly available from the macroion-macroion radial distribution function.

From general principles of local equilibrium, the mean force acting on one macroion can be expressed in an infinite number of ways.[41,42] In one of them, also being numerical advantageous, $F(r)$ is decomposed according to[7]

$$F(r) = F_{ideal}(r) + F_{elec}(r) + F_{hs}(r). \qquad (11)$$

In Eq. (11), the first term $F_{ideal}(r)$ is given by

$$F_{ideal}(r) = kT \sum_i \left[\rho_i(z=0) - \rho_i(z=L_{cyl}/2) \right] A_{cross} \qquad (12)$$

and denotes the difference in the transfer of linear moments across the planes $z=0$ and $z=L_{cyl}/2$ with $\rho_i(z=z')$ being the number density of species i in the plane $z=z'$ averaged over the cross-section area A_{cross} of the cylinder and k Boltzmann's constant. As long as $r \ll L_{cyl}/2$, $F_{ideal}(r)$ is dominated by the $\rho_i(z=0)$ term. The remaining two terms in Eq. (11) arise from interactions across the plane $z=0$. The first of them, $F_{elec}(r)$ becomes

$$F_{elec}(r) = \sum_{i<j}^{N} {}' \langle -\nabla_{r_{ij}} u_{ij}^{elec}(r_{ij}) \rangle \qquad (13)$$

and represents the average force across the plane $z=0$ originating from the electrostatic interaction among the charged species and the prime that the summation only include pairs of species located on different sides of the plane $z=0$. The other term $F_{hs}(r)$ is given by

$$F_{hs}(r) = \sum_{i<j}^{N} {}' \langle -\nabla_{r_{ij}} u_{ij}^{hs}(r_{ij}) \rangle \qquad (14)$$

and represents the averaged force across the plane $z=0$ through hard-sphere contacts.

The evaluation of $F_{ideal}(r)$ was performed according to

$$F_{ideal}(r) = -kT \lim_{\Delta h \to 0^+} \left[\frac{\langle N_I \rangle_{\Delta h}^{(0)}}{\Delta h} - \frac{\langle N_I \rangle_{\Delta h/2}^{(-)} + \langle N_I \rangle_{\Delta h/2}^{(+)}}{\Delta h} \right], \qquad (15)$$

where $\langle N_I \rangle_{\Delta h}^{(0)}$ denotes the average number of counterions in a slab with the width Δh centered at $z=0$ and $\langle N_I \rangle_{\Delta h/2}^{(\mp)}$ the average number of counterions in a slab with the width $\Delta h/2$ centered at $z= \mp (L_{cyl} - \Delta h/2)/2$. A smaller Δh provides a principally improved $F_{ideal}(r)$ but subjected to a larger statistical uncertainty, whereas a larger Δh reduces the statistical uncertainty but increases the systematic error.[7] Throughout, $\Delta h = 0.1$ Å has been used. The calculation of $F_{elec}(r)$ is straightforward. Finally, $F_{hs}(r)$ was evaluated by performing virtual displacement ($\Delta s = 0.1$ Å) of counterions near the plane $z=0$ toward the plane $z=0$ and check for hard-sphere overlap.[14]

Potentials of mean forces have also been calculated directly from simulations by sampling the frequency of the macroion separation r, $P(r)$. From $P(r)$ the pmf was constructed according to

$$U^{pmf}(r)/kT = -\ln \left[\frac{P(r)}{P(r \to \infty)} \right]. \qquad (16)$$

Here, $P(L_{cyl}/2)$ was used to normalize $U^{pmf}(r)$, i.e., $U^{pmf}(L_{cyl}/2)=0$ was assigned. In the case with monovalent
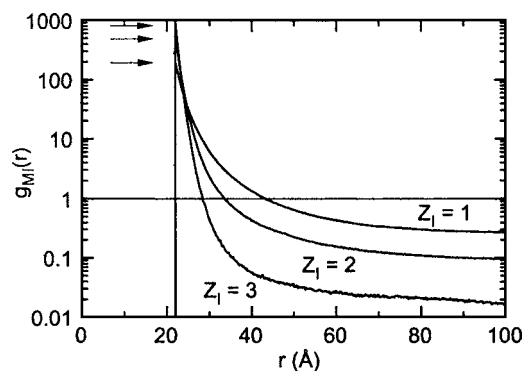
FIG. 3. Macroion-counterion radial distribution functions at indicated values of the counterion valence for the central charge distribution as obtained from the spherical cell. The arrows point on the values at $r=R_M+R_I=22$ Å. The thin horizontal line at $g_{MI}=1$ corresponds to systems of uncorrelated particles.
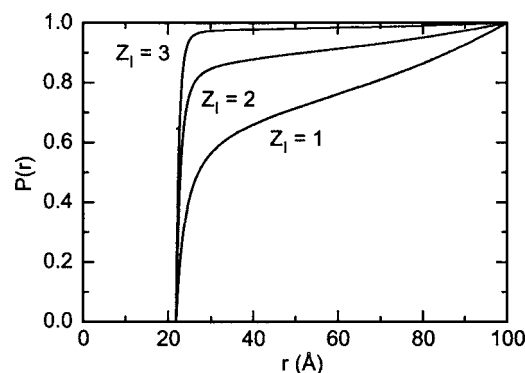

FIG. 4. Normalized counterion running coordination number at indicated values of the counterion valence for the central charge distribution as obtained from the spherical cell.

counterions, the pmf is strongly repulsive. To enable a sampling at short separations the weighting function $w(r)=A_1 \exp[-A_2(r-A_3)]$ was used with the coefficients A_1, A_2, and A_3 selected such that the $U^{pmf}(r)+w(r)$ becomes close to zero.

The mean force was evaluated from a set of simulations with different values of r and the pmf from a single, but longer, simulation. Although we have employed both routes to calculate effective macroion interactions, results mainly from the mean force route will be given.

III. RESULTS

Results for the different boundary conditions will be presented separately in different subsections. In each of these, the properties of systems with macroions possessing a central charge distribution will first be examined. Thereafter, the effects of surface and protruding macroion charges will be assessed, followed by an account of the influence of the mobility of the macroion charges.

A. Spherical cell

1. Central charge distribution

Macroion-counterion radial distribution functions (rdfs) for the central charge distribution with different counterion valences are shown in Fig. 3. Such rdfs obtained from a spherical cell describe the distribution of counterions near a single macroion that is well separated from other macroions. The function provides the relative density of small ions at distance r from the macroion, its value being unity in the absence of any spatial correlations.

Independent of the counterion valence, there is strong accumulation of the counterions near the macroion surface. The equilibrium counterion distribution is a compromise between (i) the macroion-counterion electrostatic attraction striving to a complete adsorption of the counterions on the macroion surface and (ii) the counterion entropy promoting a homogeneous counterion density. At increasing counterion valence, the macroion-counterion electrostatic increases in magnitude leading to a more uneven counterion distribution. For example, the values of g_{MI} at macroion-counterion hard-sphere contact ($r=22$ Å) are 199, 570, and 991 with $Z_I=1, 2,$

and 3, respectively. Moreover, for the present model the reduced osmotic pressure is given by the value of g_{MI} at the cell wall according to $p/\rho_I kT=g_{MI}(R_{cell})$, where ρ_I is the counterion number density. Hence, the reduced pressure decreases according to 0.27, 0.093, and 0.016 at increasing counterion valence.

The running coordination number is another important quantity that follows directly from the macroion-counterion rdf according to $rcn(r)=\rho_I \int_0^r 4\pi r'^2 g_{MI}(r')dr'$. It denotes the number of counterions within the distance r from the center of the macroion, and it possesses the limit $rcn(r) \rightarrow N_I$ as $r \rightarrow R_{sph}$. To facilitate a comparison among different counterion valences, it is more favorable to consider the normalized counterion rcn according to $P(r)=rcn(r)/N_I$ with the limit $P(r) \rightarrow 1$ as $r \rightarrow R_{sph}$, describing the fraction of counterions appearing within a distance r from the macroion center.

Figure 4 shows $P(r)$ for the central charge distribution with different counterion valences. Experimental methods such as NMR are able to probe the fraction of counterions near, say, 3 Å from the macroion surface. Using 3 Å as a distance criterion, we found with mono-, di-, and trivalent counterions that 41%, 76%, and 94%, respectively, of the counterions are at the macroion surface, again demonstrating the strong effect of the counterion valence on the association of the counterions to the macroion.

2. Different macroion charge distributions

The macroion–monovalent-counterion rdfs for the five different macroion charge models are shown in Fig. 5. Furthermore, Fig. 6 shows the difference of $P(r)$ between the discrete charge distributions and the central charge distribution.

As compared to the central charge distribution (C), Fig. 5 shows that the two representations of the surface charge distribution (FS and MS) give rise to a stronger accumulation of counterions near the macroion surface, the relative increase becoming stronger with increasing counterion valence. Regarding the two representations of the protruding charge distribution (FP and MP), the shape of $g_{MI}(r)$ becomes different; the amplitude near the macroion surface is strongly reduced and a cusp appears at $r=26$ Å, prominent with $Z_I=1$ but weaker with multivalent counterions. Figure 6 shows more clearly the increased accumulation of the coun-
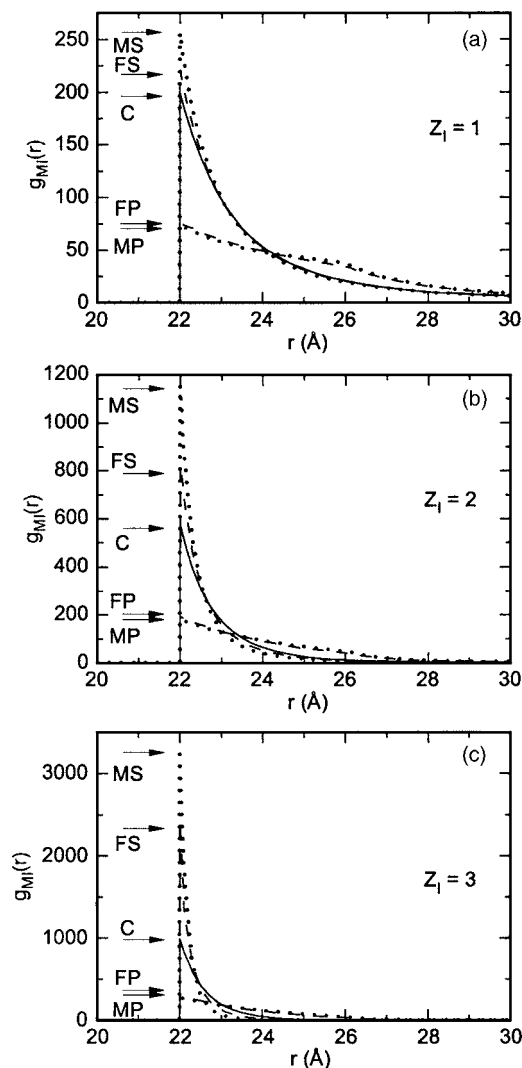
FIG. 5. Macroion-counterion radial distribution functions with counterion valences (a) $Z_I=1$, (b) $Z_I=2$, and (c) $Z_I=3$ for the central charge distribution (solid curve), frozen surface and frozen protruding charge distributions (dashed curves), and mobile surface and mobile protruding charge distributions (dotted curves) as obtained from the spherical cell.

FIG. 6. Relative normalized running coordination number for counterion valences (a) $Z_I=1$, (b) $Z_I=2$, and (c) $Z_I=3$ for the frozen surface and frozen protruding charge distributions (dashed curves) and mobile surface and mobile protruding charge distributions (dotted curves) as obtained from the spherical cell. $\Delta P(r) = P(r) - P_{\text{central charge}}(r)$.

terions for the surface charge distribution and the opposite behavior for the protruding charge distribution. Common is that the deviations from the central charge distribution is mainly localized to the nearest ≈ 10 Å from the macroion surface; for longer distances the differences in the integrated number of counterions are smaller and decreases with increasing Z_I.

The influence of the mobility of the macroion charges is smaller than the effects of their protrusion into the solution. Figure 5 shows that the accumulation of counterions near the macroion surface is larger for mobile surface charges (MS) as compared to frozen ones (FS), and Fig. 6 demonstrates that the difference of the fraction of counterions near the surface between these two surface charge arrangements increases with increasing counterion valence. Finally, the counterion distributions are nearly the same for the frozen protruding (FP) and mobile protruding (MP) charge distributions.

To conclude, the exchange of the conventional central charge distribution, equivalent to a homogeneous surface
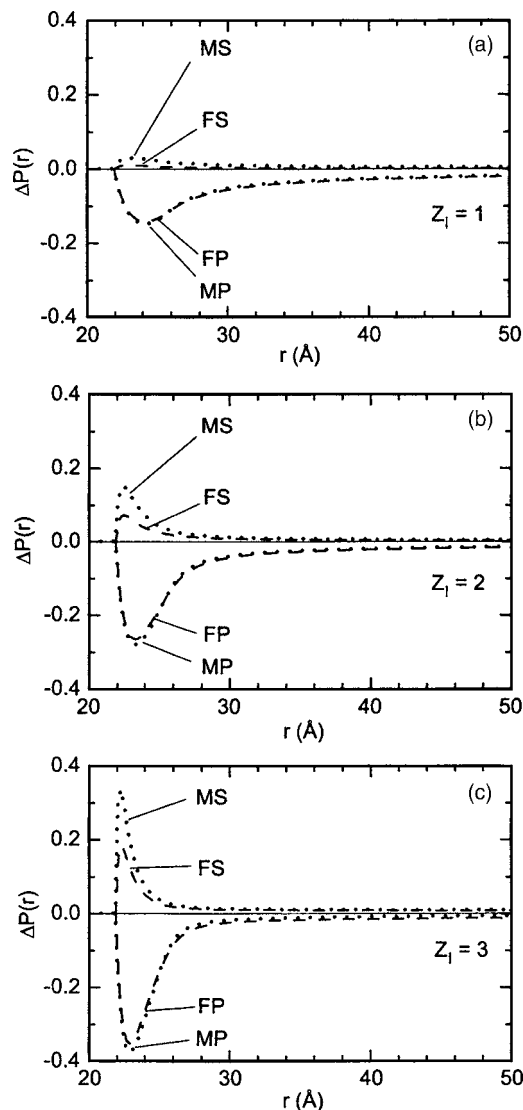
charge density, with more realistic macroion charge distributions may considerably affect the counterion distribution near a macroion. A model with discrete macroion charges enables an increased macroion-charge–counterion spatial correlation. In the case with point charges on the macroion surface, the increased macroion-charge–counterion correlation enhances the counterion accumulation. On the other hand, with protruding charges the excluded volume effect dominates over the correlation effect, and the macroion–counterion rdf displays additional features. With mobile macroion charges, the accumulation of counterions increases in the case of surface charges, but remains virtually unaffected in the case of protruding charges. The described effects become more prominent with increasing counterion valence.

The structure among the mobile macroion charges is quantified in Fig. 7, showing the macroion-charge–macroion-charge rdf using the arc length separation between pairs of macroion charges. As for three-dimensional rdfs, is normal-
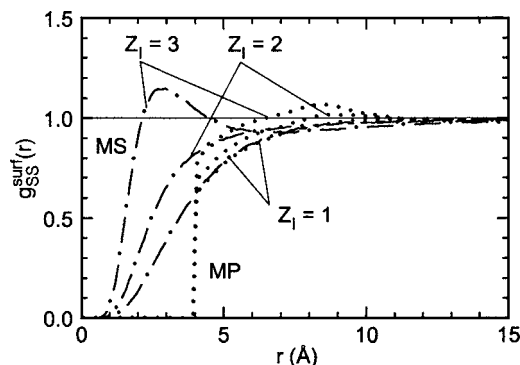
FIG. 7. Macroion charge–macroion charge radial distribution function for the mobile surface (dot-dashed curves) and mobile protruding (dotted curves) charge distributions at indicated values of the counterion valence as obtained from the spherical cell. Here, r denotes the arc length separation between pairs of macroion charges. The thin horizontal line at $g_{SS}^{surf}=1$ corresponds to systems of uncorrelated particles.

ized to unity for a uniform distribution, here on a surface of a sphere of radius r_S. At short separations, $g_{SS}^{surf}(r)<1$ implying that the macroion charges effectively repel each other. For the surface charge distribution with point charges [see Fig. 1(b), left], the short-range repulsion originates of course only from the electrostatic interactions, whereas for the protruding charge distribution with finite-sized charges ($R_s =2$ Å) [see Fig. 1(b), right], the hard-sphere repulsion is the dominating short-range interaction. Figure 7 shows that the dependence on Z_I is considerable in the former case (MS), but only moderate in the latter one (MP). The effective repulsion among the macroion charges is largest for monovalent counterions and smallest for trivalent ones. Noticeable is that with the surface charge distribution and trivalent counterions a maximum appears at 3 Å, demonstrating a clustering of the monovalent macroion charges, here driven by nearby trivalent counterions.

Thus, with increasing valence, counterions have an enhanced ability to attract two or more macroion charges and bring them close in space. This increasing ability is pronounced for point charges, but limited for the finite-sized charges due to the impeding hard-sphere repulsion among the macroion charges. In this conclusion, we conjecture that the difference in the hard-sphere radii has a larger importance than the difference in the radial position of the surface and protruding charge distributions. Finally, we relate the larger change in the macroion charge structure at increasing counterion valence observed for the surface charge distribution (MS) as compared to the protruding charge distribution (MP) shown in Fig. 7 to the likewise larger change in the radial counterion distribution displayed in Figs. 5 and 6.

B. Cylindrical cell

1. Central charge distribution

As mentioned, a cylindrical cell containing two macroions and their counterions were used to examine the effective interaction between two macroions. Figure 8(a) shows the mean force between two macroions as a function of their separation at different counterion valences as evaluated from Eqs. (9) and (11)–(15) for the central charge distribution.
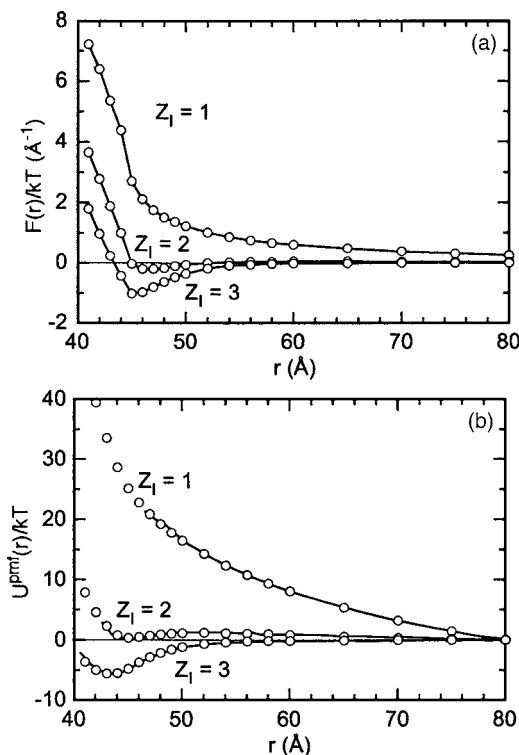

FIG. 8. (a) Reduced mean force (symbols with lines as guide) from Eqs. (9)–(15) and (b) reduced potential of mean force from Eqs. (10) (symbols) and (16) (curves) as a function of the macroion separation for the central charge distribution at indicated values of counterion valence as obtained from the cylindrical cell.

Moreover, Fig. 8(b) displays the pmf obtained from the integration of the mean force, Eq. (10), (symbols) and from the sampling of the frequencies of different macroion separations, Eq. (16), (solid curves). In the range of macroion separations visited, a virtually perfect agreement of $U^{pmf}(r)$ is found between the two different approaches involving independent sets of simulations.

With monovalent counterions, the mean force and potential of mean force are monotonous and strongly repulsive. Since the mean force is still positive at the largest separation examined, $r=80$ Å, $U^{pmf}(80$ Å$)$ has still a nonzero slope and a (unknown) vertical shift has to be applied to achieve $U^{pmf}(r)\rightarrow 0$ as $r\rightarrow\infty$. With divalent counterions, the effective long-range repulsion has almost vanished and between $r=45$ and 50 Å the mean force becomes attractive, and, consistently, the pmf display a (local) minimum at $r=45$ Å. Finally, with trivalent counterions, the mean force is nonzero only at short separation; attractive between $r=44$ and ≈ 60 Å and repulsive at $r<44$ Å. The separation 44 Å corresponds to a macroion-macroion surface separation equal to a counterion diameter. The global minimum of $U^{pmf}(r)$ at 44 Å amounts to nearly $-6kT$.

Hence, with monovalent counterions, the conventional picture of like-charged macroion displaying an effective repulsion appears. However, with trivalent counterions the picture is completely changed; now the macroions are effectively attracted to each other, the attraction being mediated by the counterions. The case with divalent counterions falls in between; a local potential minimum appears at short sepa-
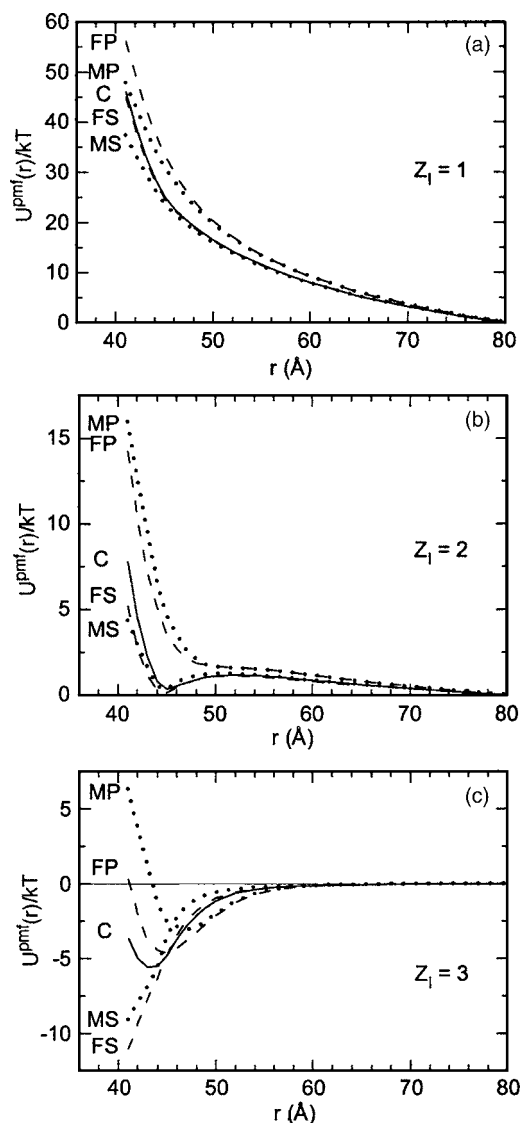
FIG. 9. Reduced potential of mean force as a function of the macroion separation from Eqs. (9)–(15) for counterion valences (a) $Z_I=1$, (b) $Z_I=2$, and (c) $Z_I=3$ for the central charge distribution (solid curves), frozen surface and frozen protruding charge distributions (dashed curves), and mobile surface and mobile protruding charge distributions (dotted curves) as obtained from the cylindrical cell.

ration. Similar mean forces and pmfs have been reported by Angelescu and Linse[24] and related effective macroion-macroion potentials with mono- and divalent counterions by Lobaskin et al.[20]

2. Different macroion charge distributions

Figure 9 displays the reduced potential of mean force as a function of the macroion separation for the three counterion valences considered and all macroion models. Regarding monovalent counterions, the pmf with the surface charge distribution (FS and MS) is strongly repulsive and nearly identical that of the central charge distribution (C). With divalent counterions, the local minimum at short separation becomes slightly more accentuated and shifted ca. 1 Å inwards and the potential rise near contact appears at shorter separation. The most prominent changes occur with the trivalent counterions; here the onset of attraction occurs at slightly shorter

separation and the minimum appearing at ≈ 44 Å for the central charge distribution is replaced with a deeper minimum essentially at macroion contact. As to the protruding charge distribution (FP and MP), the pmf becomes generally more repulsive. With divalent counterions the local minimum at ≈ 45 Å has vanished, and with trivalent counterions the global minimum becomes less deep and shifted to longer macroion separation.

The influence of the macroion charge mobility depends on the counterion valence and charge distribution. With monovalent counterions, the mobility leads to a *weaker repulsion*, but the importance of the weaker repulsion is strongly limited due to the large value of the pmf. With multivalent counterions, surface charge mobility leads to a *more repulsive/less attractive* pmf. In particular, the macroion-charge mobility reduces the magnitude of the pmf minimum appearing for the protruding charge distribution with trivalent counterions [cf. curves labeled FP and MP in Fig. 9(c)].

We will now consider the distributions of the macroion charges and counterions along the C_∞ axis of the cylinder. Volume densities averaged over cylindrical cross sections as a function of the z coordinate, $\rho_i(z)$, at macroion separations $r=46$, 60, and 80 Å have been determined. Note, by symmetry $\rho_i(-z)=\rho_i(z)$ and by geometry, the volume density of the macroion charge at a given z coordinate is proportional to the density of surface charges at that z coordinate.

Figure 10 displays the volume charge density $|Z_i|\rho_i(z)$ for the central and mobile surface charge distributions at macroion separation $r=46$ Å. With $Z_I=2$ and 3, an attractive mean force appears at this separation. For a homogenous surface charge distribution, $|Z_s|\rho_s(z)$ is zero for $|z|<3$ Å or $|z|>43$ Å and attains the value $|Z_s|N_s/2\pi R_{cyl}^2 R_M=7.36 \times 10^{-5}$ Å^{-3} for 3 Å $\leq|z|\leq 43$ Å. A polarization of the surface charges appears at $r=46$ Å (dotted curves labeled S); with monovalent counterions surface charges are displaced *from* the area close to the other macroion and with multivalent counterions they are displaced *to* the area close to the other macroion. The changes of the surface charge density at $z=3$ Å (corresponding to the point closest to the other macroion) are -21%, $+32\%$, $+63\%$ for $Z_I=1$, 2, and 3, respectively. The size of the areas with markedly charge polarization is small.

The corresponding counterion charge densities $|Z_I|\rho_I(z)$ between $z=3$ and 43 Å are smaller than $|Z_s|\rho_s(z)$, since counterions are also able to explore the region outside this interval. This charge density difference becomes smaller with increasing counterion valence due to the larger association of the counterions to the macroion earlier discussed. With monovalent counterions, there is a high counterion density in a region centered at $z=0$ and extending ca. 10 Å in either direction due to the overlapping counterion distributions originating from the two macroions. With increasing counterion valence, the extension of the region with high counterion density becomes smaller.

There are two characteristic differences in the counterion charge density profiles between the central and mobile surface charge distributions. For the latter distribution, (i) a lower counterion concentration near $z=0$ appears and (ii) a lower ($Z_I=1$) or higher ($Z_I=2$ and 3) counterion concentra-
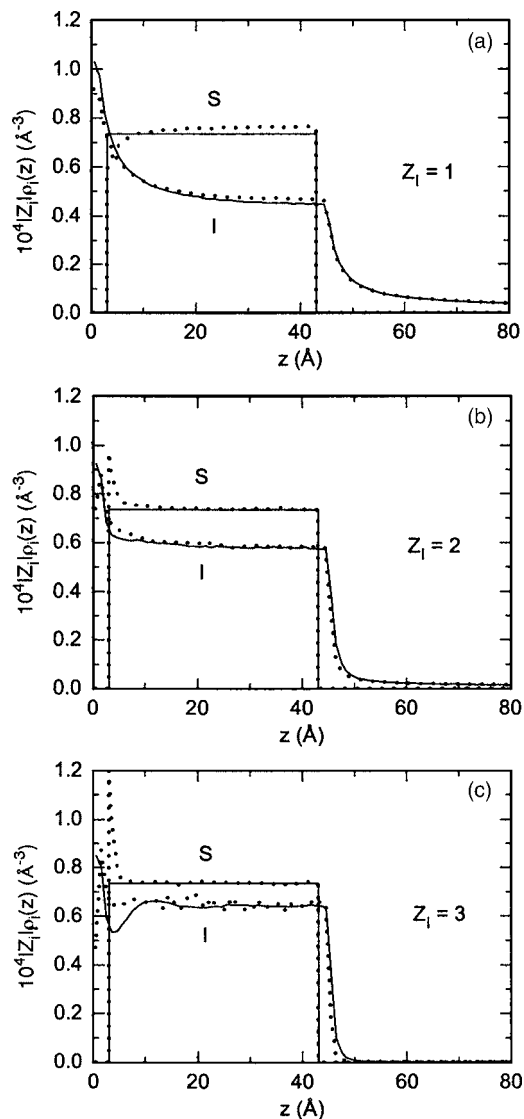
FIG. 10. Volume charge density of macroion charges (labeled S) and counterions (labeled I) as a function of the z coordinate for counterion valences (a) $Z_I=1$, (b) $Z_I=2$, and (c) $Z_I=3$ for the central (solid curves) and the mobile surface (dotted curves) charge distributions at macroion separation $r=46$ Å as obtained from the cylindrical cell. The charge density is averaged over the circular cross section of the cylindrical cell.

tion in the interval $z \approx 2-10$ Å occur, the latter following the surface charge polarization of the mobile surface charge distribution.

At the macroion separation $r=60$ Å, a weak surface charge polarization remains with $Z_I=1$ but has vanished with $Z_I=2$ and 3 (data not shown). At $r=80$ Å and $Z_I=1$, the counterion distributions of the two macroions are still considerably overlapping.

To conclude, with monovalent counterions the influence of the macroion charge distribution becomes sizable at short separations, at which the effective macroion-macroion repulsion anyhow is very strong. For example at $r=46$ Å the pmf is reduced from 22.8 (central charge distribution) to 21.7kT (mobile surface charge distribution), and we related this reduced repulsion with the depletion of surface charges in the area close to the other macroion. With multivalent counterions, where the effective macroion-macroion interaction can

become attractive, the details of the macroion charge distribution have a larger qualitative impact on the macroion-macroion pmf. With mobile surface charges, the charges are displaced to the macroion-macroion contact region and enforce the attractive spatial correlation among the surface charges and counterions. Protruding macroion charges result in a purely repulsive (divalent counterions) or less attractive (trivalent counterions) pmf.

C. Cubic box

Simulations of bulk solutions of macroions and counterions provide a wealth of structural and thermodynamic information. Here, we will focus on the spatial distributions of the macroions by employing macroion-macroion rdfs and macroion-macroion structure factors. The latter is defined according to

$$S_{MM}(q) \equiv \left\langle \frac{1}{N_M} \left| \sum_{i=1}^{N_M} \exp\left(i\mathbf{q} \cdot \mathbf{r}_i\right) \right|^2 \right\rangle, \tag{17}$$

where $\mathbf{q}$ denotes the wave vector with the magnitude q, $\mathbf{r}_i$ the position of macroion i and $\langle \cdots \rangle$ an ensemble average. It should be noted that the lower limit q_{low} of the wave vector is controlled by the box size according to $q_{low}=2\pi/L_{box}$ (≈ 0.012 Å^{-1}). The structure factor is useful for assessing the stability of a system. An increase of S as q approaches zero implies an appearance of density fluctuations at long length scales, revealing an effective attraction among the macroions. In a finite system, $S_{MM}(q \to 0)$ always remains finite, and it approaches N_M when all the macroions form a single cluster. Structure factors and radial distribution functions are related through a three-dimensional Fourier transform, and, thus, contain the same information. Nevertheless, the two quantities emphasize different aspects of the structure.

1. Central charge distribution

Selected macroion-macroion rdfs and structure factors for the central charge distribution (C) with different counterion valences are shown in Figs. 11 and 12, respectively. With monovalent counterions, Fig. 11(a) displays that the macroions are always well separated and a maximum appears at $\rho_M^{-1/3}$, indicating an effectively strong repulsion among the macroions. With divalent counterions, Fig. 11(b) shows that spatial correlations remain only up to ≈ 150 Å, indicating an attenuated repulsion, and the peak appearing at ≈ 45 Å suggests a local potential minimum at that separation. Finally, with trivalent counterions the macroion-macroion structure factor given in Fig. 12 displays a strong increase at decreasing wave vector q. Moreover, $S_{MM}(q)$ at small q is consistent with the form factor of a hard sphere with a radius of $\approx 5R_M$ and an amplitude of 40 at $q=0$. Hence, we conclude that the macroions form a single cluster and the solution is not stable at those conditions.

These findings at different counterion valences are (i) similar to those results obtained for a higher number density and a system comprising 80 macroions[15] and (ii) in consistence with the pmfs given in Fig. 8(b). It has previously been shown that macroion-macroion pmfs extracted from bulk solutions according to $U^{pmf,bulk}(r) \equiv -kT \ln[g_{MM}^{bulk}(r)]$ are close

FIG. 12. Macroion-macroion structure factor with trivalent counterions for the central charge distribution (solid curve) and the frozen surface and frozen protruding charge distributions (dashed curves). The thin horizontal line at $S_{MM}=1$ corresponds to a system of uncorrelated macroion. The thin solid curve displays 40 times the form factor P_{HS} of a hard sphere with radius $5R_M$. $P_{HS}(x)=[3j_1(x)/x]^2$, where j_1 denotes the spherical Bessel function of the first order.

cylindrical cell approach [see Fig. 9(a)] and the smaller accumulation of counterions to the macroion [see Fig. 6(a)].

With divalent counterions, Fig. 11(b) displays that the effect of the charge distribution on $g_{MM}(r)$ becomes larger, which mainly is a consequence of the smaller magnitude of the effective macroion-macroion interaction. In the case of the frozen surface charge distribution (FS), the peak at ≈ 45 Å is increased in magnitude, consistent with the deeper minimum in the pmf [see Fig. 9(b)]. Moreover, the peak at ≈ 45 Å has vanished for the frozen protruding charge distribution (FP) and the rise is shifted to a larger macroion separation, both aspects consistent with the differences between the pmf for the central and frozen protruding charge distributions [see Fig. 9(b)].

Finally, with trivalent counterions, the charge distribution plays an important role. For the frozen surface charge distribution, $S_{MM}(q)$ given in Fig. 12 displays a large rise at low q, similar to that for the central charge distribution, demonstrating an unstable solution. For the frozen protruding charge distribution, $S_{MM}(q)$ display only a weak increase at low q, hence signaling much milder density fluctuations. The corresponding $g_{MM}(r)$ given in Fig. 11(c) displays a sharp peak at $r=47$ Å and a secondary one ≈ 85 Å. In addition, a cluster size analysis (see the Appendix for details) gives an average cluster size of four macroions. Thus, for the frozen protruding charge distribution, an effective attraction among the macroions is present, but not sufficiently strong to cause a phase instability. Again, the results from the bulk simulations are consistent with the pmfs, which for trivalent counterions displayed a deep minimum at macroion contact for the surface charge distribution, whereas the absolute value of the minimum $-4.6kT$ for the protruding charge distribution is smaller than the absolute value of $-5.7kT$ for the central charge distribution [see Fig. 9(c)].

Hence, we infer from our results that the binodal curve separating thermodynamic stable and unstable solutions is markedly dependent on the precise nature of the macroion charge distribution. With increasing possibility of spatial correlations between macroion charges and counterions, the ef-
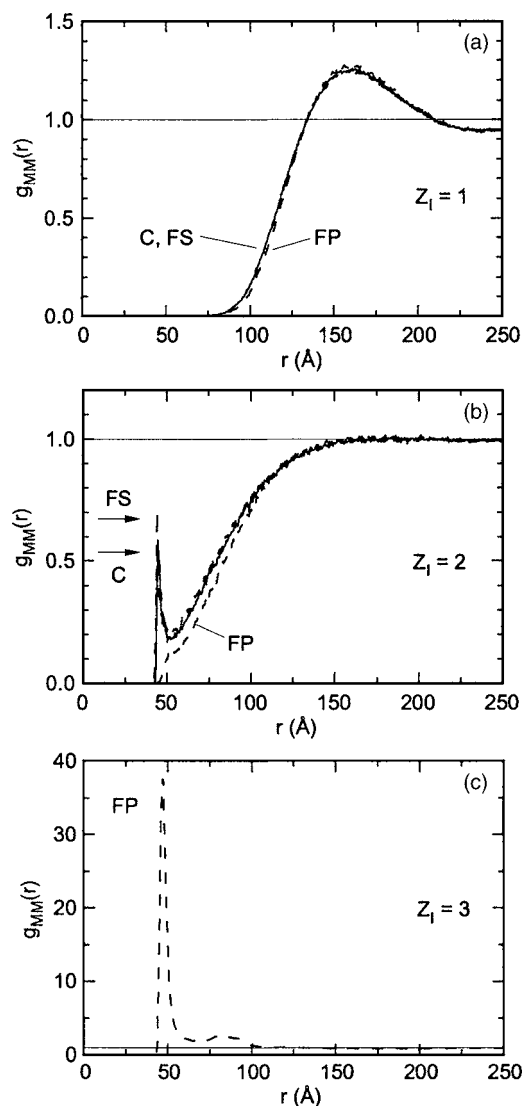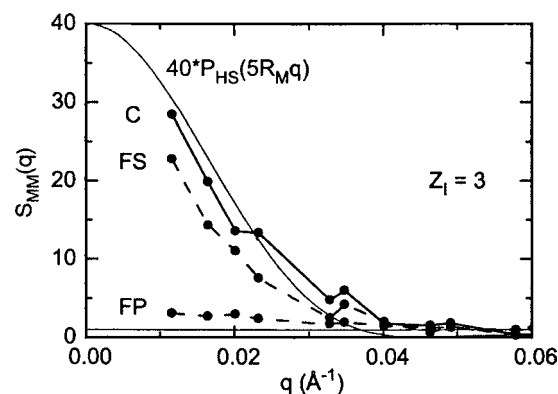

FIG. 11. Selected macroion-macroion radial distribution function for counterion valences (a) $Z_I=1$, (b) $Z_I=2$, and (c) $Z_I=3$ for the central charge distribution (solid curves) and the frozen surface and frozen protruding charge distributions (dashed curves). In (c), the rdf is only given for the frozen protruding charge distribution. The thin horizontal lines at $g_{MM}=1$ corresponds to systems of uncorrelated macroion.

to $U^{pmf}(r)$ obtained from two macroions and their counterions enclosed in a cylindrical cell under various conditions.[22]

2. Different macroion charge distributions

The influence of the macroion charge mobility was previously shown to be smaller than the effect of having a discrete charge distribution. Hence, here the comparison will be focused on the central and surface charge distributions.

With monovalent counterions, Fig. 11(a) shows that the influence of the macroion charge distribution on the macroion-macroion rdf is small. For the frozen surface charge distribution (FS), $g_{MM}(r)$ is indistinguishable from that for the central charge distribution (C) within the statistical uncertainty. For the protruding charge distribution (FP) the rise of $g_{MM}(r)$ appears at slightly larger separation consistent with the more repulsive pmf as obtained from the

fective macroion-macroion attraction mediated by the counterions is increased and the instability region becomes larger. When the macroion charges protrude into the solution, while keeping the macroion hard-sphere radius fixed, the correlations are weakened and the extension of the unstable region becomes smaller. As in previous studies,[22] we find a good correspondence between macroion-macroion pmfs evaluated in a cylindrical cell and macroion-macroion rdfs obtained from bulk solutions.

IV. SUMMARY

On the basis of Monte Carlo simulations, properties of aqueous solutions containing macroions and counterions have been determined for models involving representations of the macroion charges. Beside the conventional central charge model, discrete models including point charges localized on the macroion surface and finite-sized charges protruding into the solution have been considered. The strongest charge-charge correlation effects for a smooth macroion surface are expected with the former model, whereas the latter one is likely more realistic. Moreover, both frozen and mobile macroion charges were examined and mono-, di-, and trivalent counterions were employed. Three different boundary conditions were used.

The distribution of counterions near a macroion and the macroion structure were determined using a spherical cell, whereas the mean force and the potential of mean force operating on a macroion as well the longitudinal distribution of the counterions were determined using a cylindrical cell containing two macroions and their counterions. Finally, a cubic box was used to determine the structure and stability of bulk solution.

Our main findings and conclusions are as follows:

(A) The effect of the change from the central charge distribution, equivalent to a homogenous surface charge density, to different discrete charge distributions became more pronounced as the counterion valence is increased.

(B) With point charges at the macroion surface, an increased accumulation of counterions near the macroion was observed, which lead to a reduced effective macroion-macroion repulsion (divalent counterions) and an increased effective macroion-macroion attraction (trivalent counterions).

(C) With macroion charges protruding beyond the constant macroion hard-sphere radius, the excluded volume effect gave rise to a reduced accumulation of counterions near the macroion, which increased the effective macroion-macroion repulsion (monovalent counterions), made the effective macroion-macroion repulsive (divalent counterions), and reduced the effective macroion-macroion attraction (trivalent counterions).

(D) The influence of the macroion charge mobility was mostly smaller than the effect of a discrete charge distribution. With monovalent counterions a depletion of macroion charges from the macroion-macroion contact region lead to a weaker effective macroion-macroion repulsion, whereas with multivalent counterions an ac-

cumulation of macroion charges to the contact region made the effective macroion-macroion attraction repulsive (divalent counterions) or less attractive (trivalent counterions).

(E) With trivalent counterions, the phase instability region increased for surface charges and decreased with protruding charges.

The construction of a macroion model beyond the conventional one involving a charge placed in a hard sphere possesses several challenges. Two of these issues have here been considered: the role of discrete charge distributions and the mobility of the macroion charges for a model representing micelles formed by charged surfactants. We expect the outcome of our investigation to depend on the particular charged colloid of interest through the surface charge density and size of the protruding charged groups. For example, here the electrostatic coupling between neighboring macroion charges is $\approx 1kT$; at a lower coupling we expect the role of charge mobility to be enhanced.

ACKNOWLEDGMENT

APPENDIX: EQUILIBRATION OF THE 60-3 SYSTEMS

In previous simulation studies,[15,17] it has been concluded that at the present conditions a solution of macroions with a central charge distribution and trivalent counterions confined in a cubic box with periodic boundary conditions possesses a miscibility gap. Since attractive pmfs were obtained from the cylindrical cell simulations for the other charge distributions as well, phase instability might appear also for these distributions. In the following, we will give a more detailed account of trial displacements used in the MC simulations and the equilibration of these solutions.

In addition to cluster moves involving simultaneous trial displacement of the macroions and neighboring counterions, macroions were also subjected to a second-level cluster move.[7] This type of trial move involves a simultaneous trial displacement of the selected macroion, other macroions belonging to the same cluster, and neighboring counterions to all macroions belonging to the cluster. Two macroions are considered to belong to the same cluster if they are "connected" directly or indirectly through one or several other macroions. Two macroions are treated as directly connected if their center-of-mass separation does not exceed 46 Å. At those conditions where smaller clusters are present, the second-level cluster move enable the small clusters to move close to each other. In the present protocol, where the second-level cluster trial move is rejected if the trial move would lead to a change in the number of macroions in a cluster (a simple way to ensure the detailed balance condition), the merging of two clusters or the splitting of a single cluster is achieved by the cluster move involving just one macroion and its counterions. The process of merging of two
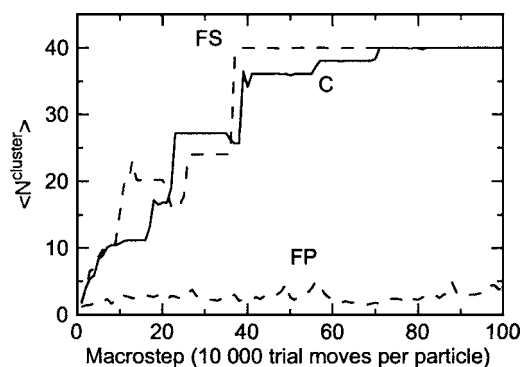
FIG. 13. Average cluster size as a function of the macrostep of the equilibration involving 10^6 trial moves per particle with trivalent counterions for the central (solid curve), frozen surface (short-dashed curve), and frozen protruding (long-dashed curve) charge distributions. See text for the evaluation of the average cluster size. The translational displacement parameter of the cluster move was 15 Å, and counterions within 26 Å from the center of a macroion were included in a cluster move. Regarding the second-level cluster move, the translation displacement parameter was also 15 Å and macroions separated at most 46 Å were considered as connected.

clusters by successive transfer of single macroions through the intervening solution is extremely slow.

A convenient way to follow solution stability during the equilibration is to examine the formation of macroion clusters. In the cluster size analyses, two macroions are treated as directly connected if their center-of-mass separation does not exceed 50 Å. From the simulations, the cluster size probability distribution P_m was calculated according to $P_m = m\langle N_m^{cluster}\rangle / \Sigma_m m\langle N_m^{cluster}\rangle$, where $\langle N_m^{cluster}\rangle$ is the average number of clusters containing m macroions and the denominator is equal to the number of macroions N_M by number conservation. Note that P_m is a "mass-"weighted measure of the cluster size distribution, where the *number* of macroions m in a cluster provides the weight. The probability P_m represents the probability that any randomly chosen macroion will be found in a cluster with m macroions. From P_m the average cluster size $\langle N^{cluster}\rangle$ was evaluated according to $\langle N^{cluster}\rangle = \Sigma_m m P_m$.

Figure 13 displays the development of $\langle N^{cluster}\rangle$ during extended equilibration runs with the central surface charge distribution and the frozen surface and frozen protruding charge distributions. We recall that random initial distributions of the charged species were used. It is observed that in the case of the central and surface charge distributions all macroions form a single cluster after 70 and 40 macrosteps, respectively. With protruding macroion charges the average cluster size remains three to four throughout.

[1] D. F. Evans and H. Wennerström, *The Colloidal Domain Where Physics, Chemistry, Biology, and Technology Meet* (VCH, New York, 1994).
[2] *Ordering and Phase Transitions in Charged Colloids*, edited by A. K. Arora and B. V. R. Tata (VCH, New York, 1996).
[3] V. Vlachy, Annu. Rev. Phys. Chem. **50**, 145 (1999).
[4] J.-P. Hansen and H. Löwen, Annu. Rev. Phys. Chem. **51**, 209 (2000).
[5] L. Belloni, J. Phys.: Condens. Matter **12**, R549 (2000).
[6] L. B. Bhuiyan, V. Vlachy, and C. W. Outhwaite, Int. Rev. Phys. Chem. **21**, 1 (2002).
[7] P. Linse, Adv. Polym. Sci. (to be published).
[8] B. V. Derjaguin and L. Landau, Acta Physicochim. URSS **14**, 633 (1941).
[9] E. J. Verwey and J. T. G. Overbeek, *Theory of the Stability of Lyophobic Colloids* (Elsevier, Amsterdam, 1948).
[10] L. Guldbrand, B. Jönsson, H. Wennerström, and P. Linse, J. Chem. Phys. **80**, 2221 (1984).
[11] R. Kjellander and S. Marcelja, Chem. Phys. Lett. **112**, 49 (1984).
[12] E. Allahyarov, I. D'Amico, and H. Löwen, Phys. Rev. Lett. **81**, 1334 (1998).
[13] N. Grønbech-Jensen, K. M. Beardmore, and P. Pincus, Physica A **261**, 74 (1998).
[14] J. Wu, D. Bratko, and J. M. Prausnitz, Proc. Natl. Acad. Sci. U.S.A. **95**, 15169 (1998).
[15] P. Linse and V. Lobaskin, Phys. Rev. Lett. **83**, 4208 (1999).
[16] J. Wu, D. Bratko, H. W. Blanch, and J. M. Prausnitz, J. Chem. Phys. **111**, 7084 (1999).
[17] P. Linse and V. Lobaskin, J. Chem. Phys. **112**, 3917 (2000).
[18] B. Hribar and V. Vlachy, Biophys. J. **78**, 694 (2000).
[19] P. Linse, J. Chem. Phys. **113**, 4359 (2000).
[20] V. Lobaskin, A. Lyubartsev, and P. Linse, Phys. Rev. E **63**, 020401 (2001).
[21] L. Belloni, J. Phys.: Condens. Matter **14**, 9323 (2002).
[22] P. Linse, J. Phys.: Condens. Matter **14**, 13449 (2002).
[23] V. Lobaskin and K. Qamhieh, J. Phys. Chem. B **107**, 8022 (2003).
[24] D. G. Angelescu and P. Linse, Langmuir **19**, 9661 (2003).
[25] A. Naji and R. R. Netz, Eur. Phys. J. E **13**, 43 (2004).
[26] B. Jönsson, O. Edholm, and O. Teleman, J. Chem. Phys. **85**, 2259 (1986).
[27] S. Balasubramanian, S. Pal, and B. Bagchi, Curr. Sci. **84**, 428 (2003).
[28] P. Linse, J. Phys. Chem. **90**, 6821 (1986).
[29] F. L. B. da Silva, D. Bogren, O. Söderman, T. Åkesson, and B. Jönsson, J. Phys. Chem. **106**, 3515 (2002).
[30] R. Messina, J. Chem. Phys. **117**, 11062 (2002).
[31] R. Messina, C. Holm, and K. Kremer, Eur. Phys. J. D **4**, 363 (2001).
[32] R. Messina, Physica A **308**, 57 (2002).
[33] S. Linse, B. Jönsson, and W. J. Chazin, Proc. Natl. Acad. Sci. U.S.A. **92**, 4748 (1995).
[34] F. Carlsson, M. Malmsten, and P. Linse, J. Phys. Chem. B **105**, 12189 (2001).
[35] V. Lobaskin and P. Linse, J. Chem. Phys. **109**, 3530 (1998).
[36] P. Ewald, Ann. Phys. **64**, 253 (1921).
[37] M. P. Allen and D. J. Tildelsley, *Computer Simulation of Liquids* (Oxford, New York, 1987).
[38] V. Lobaskin and P. Linse, J. Chem. Phys. **111**, 4300 (1999).
[39] P. Linse and V. Lobaskin, in *Simulation and Visualization on the Grid*, edited by B. Engquist, L. Johnsson, M. Hammill, and F. Short (Springer, Berlin, 2000), Vol. 13, p. 165.
[40] P. Linse, MOLSIM (Lund University, Lund, Sweden, 2004).
[41] L. D. Landau and E. M. Lifshitz, *Electrodynamics of Continuous Media* (Pergamon, Bristol, 1960).
[42] W. B. Russel, D. A. Saville, and W. R. Schowalter, *Colloidal Dispersions* (Cambridge University Press, New York, 1989).